Advances in Water Resources 175 (2023) 104407

Contents lists available at ScienceDirect

Advances in Water Resources

journal homepage: www.elsevier.com/locate/advwatres

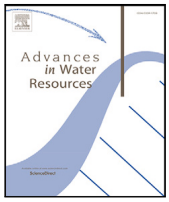

4D tomography reveals a complex relationship between wormhole advancement and permeability variation in dissolving rocks

Max P. Cooper [a,*], Rishabh P. Sharma [a,b], Silvana Magni [a,b], Tomasz P. Blach [c], Andrzej P. Radlinski [c], Katarzyna Drabik [d], Alessandro Tengattini [e,f], Piotr Szymczak [a,*]

[a] Institute of Theoretical Physics, Faculty of Physics, University of Warsaw, Warsaw, Poland
[b] Institute of Geophysics, Polish Academy of Sciences, Warsaw, Poland
[c] University of New South Wales, Minerals and Energy Resources Engineering, Sydney, Australia
[d] Oil And Gas Institute - National Research Institute, Krakow, Poland
[e] University Grenoble Alpes, CNRS, Grenoble INP, 3SR, 38000 Grenoble, France
[f] Institute Laue-Langevin, 71 avenue des Martyrs - CS 20156, 38042 Grenoble Cedex 9, France

ARTICLE INFO

Dataset link: https://doi.org/10.5281/zenodo.7558135, https://doi.org/10.5281/zenodo.7683242

Keywords:
Reactive flow
Limestone dissolution
Permeability
4D X-ray microtomography

ABSTRACT

Dissolution of porous media induces positive feedback between fluid transport and chemical reactions at mineral surfaces, leading to the formation of *wormhole*-like channels within the rock. Wormholes provide highly efficient flow and transport paths within rock, and as such, understanding their formation is critical for controlling contaminant migration or preventing CO_2 leakage during geological carbon sequestration. Here, using time-resolved X-ray tomography, we capture the dynamics of wormhole propagation, inaccessible by standard experimental methods. We find a highly non-trivial relationship between wormhole advancement and variations in permeability of the rock, with extensive periods of steady advancement not reflected by significant change in permeability. This is in contrast to most existing conceptual models where wormholes advance in a linear fashion. We show that this is caused by the presence of highly cemented regions which act as barriers to flow, as confirmed by multi-scale analysis of the pore geometry based on tomographic, (ultra) small angle neutron scattering, and optical microscopy measurements. These results demonstrate that time-lapse captured wormhole dynamics can be used to probe the internal structure of the rock.

1. Introduction

Wormholes are intricate, ramified channels formed due to dissolution of a soluble rock within a range of chemical and flow conditions. Wormholes were first described by petroleum engineers (Rowan, 1959), who injected acid into oil wells to increase reservoir permeability, allowing oil and gas to migrate more readily. A more detailed investigation of this process followed, usually accompanied by flow-through experiments in rock cores and fractures (Daccord, 1987; Hoefner and Fogler, 1988; Fredd and Fogler, 1998; Buijse, 1997; Golfier et al., 2002; Detwiler et al., 2003; McDuff et al., 2010; Li et al., 2019). Recently, understanding of wormholing became important when assessing and mitigating the risk of leakage from potential CO_2 sequestration sites, particularly in limestone formations (Ott and Oedai, 2015; Snippe et al., 2020; Luquot and Gouze, 2009; Garcia-Rios et al., 2014, 2015; Smith et al., 2013; Hao et al., 2013; Steefel et al., 2013; Elkhoury et al., 2013; Selvadurai et al., 2017; Al-Khulaifi et al., 2019). Carbon dioxide, when mixed with water, becomes aggressive and can dissolve carbonate seams or veins in the cap rock, creating CO_2 escape conduits during the sequestration process.

In addition to their practical importance, wormholes are impressive examples of a pattern-forming system driven by a strong, nonlinear coupling between flow rate, reactive transport, and evolving geometry of channels. At the large scale, wormholing processes play a major role in the formation of cave passages and karst conduit networks (Szymczak and Ladd, 2009), surface karst features such as solution pipes (Lipar et al., 2021) but also melt migration (Daines and Kohlstedt, 1994; Aharonov et al., 1995; Kelemen et al., 1995; Spiegelman et al., 2001), terra rosa formation (Merino and Banerjee, 2008), and dolomitization (Koeshidayatullah et al., 2021). Similar phenomena are involved in the formation and evolution of other branched structures, including leaf venation, river networks, and even vascular systems (Fleury et al., 2013).

The growth of wormholes is usually shielded from our eyes, due to rock mass surrounding the structure. The first studies of wormholing were then limited to observing the openings at the inlet and outlet

* Corresponding author.
E-mail addresses: max.philip.cooper@gmail.com (M.P. Cooper), piotrek@fuw.edu.pl (P. Szymczak).

https://doi.org/10.1016/j.advwatres.2023.104407
Received 16 October 2022; Received in revised form 11 January 2023; Accepted 17 February 2023
Available online 21 February 2023

side of the sample where the channels emerged. A step forward was to cast Wood's metal into the formed wormhole, use tomographic imaging techniques, or a combination of the two (Daccord, 1987; Daccord and Lenormand, 1987; Hoefner and Fogler, 1988). This allowed the visualization of the final network of wormholes formed in a rock as a result of acidization, although the understanding of the growth dynamics was limited to measuring change in pressure/permeability over the sample through the experiment. These studies established that the geometry of the wormholes strongly depends on the flow rate of the fluid that etches the rock (Hoefner and Fogler, 1988; Fredd and Fogler, 1998; Daccord et al., 1989; Golfier et al., 2002; Cohen et al., 2008). At relatively low flow rates, typically, one bulky wormhole forms within the sample. This type of wormhole is conical in shape, tapering towards the downstream end. At higher flow rates, wormholes become thinner and more tortuous, with a clear, dominant flow path through the sample. Finally, at high injection rates, wormholes become more ramified with a network of alternative flow paths spanning the sample uniformly.

Alas, these studies did not reveal the dynamics of the wormholing process itself beyond measuring macroscopic permeability evolution. Building on the use of X-ray techniques, a way forward here is to use time-lapse (4D) tomography, which requires placing the reactive flow core holder inside a tomograph. The pioneering study of this kind was performed by Bazin et al. (1996), however, due to technology of the time, acquisition times were long compared to wormhole growth, thus imaging was limited to only a few, low resolution, 2D scans (i.e., radiographs) through the sample. Recently, this technique has been used more frequently for wormhole studies (Ott and Oedai, 2015; Al-Khulaifi et al., 2019; Menke et al., 2018; Snippe et al., 2020), although with limited time resolution (~30 min), and usually only a few 3D scans per experiment. By finding a compromise between the resolution and acquisition time, we are able to make a detailed, time-resolved study of growing wormholes, with as many as ~130 (Supplementary Material, Sec. 1) scans per experiment and scan times down to five minutes. This has given us an unprecedented insight into the progressive development of wormholes through the sample.

It is worth mentioning that the dynamics of dissolution process can also be studied with another non-invasive method, Nuclear Magnetic Resonance (NMR) (Muljadi et al., 2018; Oliveira et al., 2021; Elsayed et al., 2023). NMR studies allow for the measurement of the displacement of water molecules associated with the flow through the porous rock. In this way one can quantify the evolving flow in a dissolving sample.

2. Materials and methods

To interpret wormhole propagation through limestone cores we employ 4D tomography, image processing, a simplified numerical model, and rock characterization with thin sections and scattering techniques (small and ultra-small neutron scattering). This section provides a summary of experimental methods. Full details of methods employed such as image analysis and the numerical model are presented in Appendix A.

2.1. Rock description and preparation

The rock used in this study is Pinczów Limestone (a local variety of the wider ranged Leitha Limestone), obtained from a quarry in Podłęże, Poland. Pinczów Limestone has well described facies (Studencki, 1988), and petrographic and mechanical properties (Figarska-Warchoł and Stańczak, 2019). The variety of Pinczów Limestone from this location corresponds to "type 100" as described by Figarska-Warchoł and Stańczak (2019). Pinczów/Leitha Limestone is of Middle Miocene age, and has undergone little diagenesis, limited to cementation and in some regions recrystallization of calcite. Due to limited diagenesis, it has high primary porosity (ca. 25%–35%) and permeability for a limestone. It is a packstone with grains dominated by foraminifera as well as echinoid spines, and mud consisting of calcite and approximately 10% insoluble minerals. Solubles consist of approximately 60% clay and cement and 40% grains with sizes ranging from 5 μm up to several millimeters. Mean grain size for the dominant grains, foraminifera, is 0.5 mm. Of note, horizontal laminae and recrystallized 1 mm thick zones parallel to bedding were observed by Figarska-Warchoł and Stańczak (2019).

For dissolution experiments cores 38.3 mm in diameter were prepared on a drill press using a coring bit. Cores used in dissolution experiments were scanned with high resolution X-ray tomography before each experiment. For further characterization one core was first imaged with X-ray tomography at a resolution of 30 μm, followed by thin sectioning at 10, 20, 30, 35, 50, 60, 70, and 80 mm from a core face. An additional, axially oriented thin section was prepared from 0–40 mm. Details of thin section analysis methods are presented in A.3.

Samples were also prepared for (ultra) small angle neutron scattering ((U)SANS) by crushing and sieving grains in the range $0.178 < R < 0.213$ mm, where R is the grain radius. (U)SANS measurements were performed using the SANS instrument D11 and USANS instrument S18 at the Institut Laue Langevin, Grenoble. Details on (U)SANS measurements are given in A.4.

2.2. Time-lapse dissolution-tomography experiments

Dissolution experiments were performed on limestone cores with the classic core flooding apparatus (A.2), e.g., Fredd and Fogler (1998). The core holder used (Phoenix Instruments) supports cores 38.3 mm diameter and up to 140 mm in length. The core in the experiment presented here is 115 mm long, dissolved with 0.25M hydrochloric acid at a flow rate of 1mL/min. Prior to dissolution this core was scanned at a resolution of 30 μm.

During the dissolution experiment time-lapse (4D) tomography was performed on the dissolving core at 169 μm resolution, so chosen as to balance acquisition time and the ability to pick out the advancing tip of the wormhole (details on how this value was chosen is presented in A.2 and Supplementary Material Section 3). At this spatial resolution the imaging time is ca. 5 min. Pressure drop across the cell was logged at an interval of 10 s.

An additional benchtop experiment showing characteristic pressure drop over time for Pinczów Limestone is shown in Supplementary Material, Sec. 1, along with another 4D experiment performed on the combined neutron and X-ray tomography (NeXT) instrument at Institut Laue-Langevin, Grenoble. In the additional 4D experiment 126 4D scans were taken of a dissolving, 58.7 mm long core, with a voxel size of 43.5 μm, and a temporal resolution of 7 min 20 s. The acid used in this experiment was 0.1M HCl dissolved in D_2O, and the acidization flow rate was 0.5 mL/min.

Processing of static, high resolution tomography and dynamic 4D imagery is detailed in A.3, along with processing of thin section imagery.

3. Results

3.1. 4D tomography and permeability evolution

Fig. 1 (and associated Videos S1 and S2) shows wormhole development in five minute scanning increments with a 169 μm voxel resolution. The wormhole shown here was formed in a core taken perpendicular to bedding of the relatively porous Pińczów Limestone (primary porosity ca. 25%–35% Figarska-Warchoł and Stańczak, 2019) from Pińczów, Poland, flushed with 0.25M hydrochloric acid at a flow rate of 1 mL/min. At such a flow rate, a single wormhole forms in a sample, in which most of the flow focuses. It is the so-called dominant wormhole regime according to the classification of Fredd and Fogler (1998), with the extent of the wormhole controlling the permeability of the sample. The wormhole progress is highly nonuniform, with a

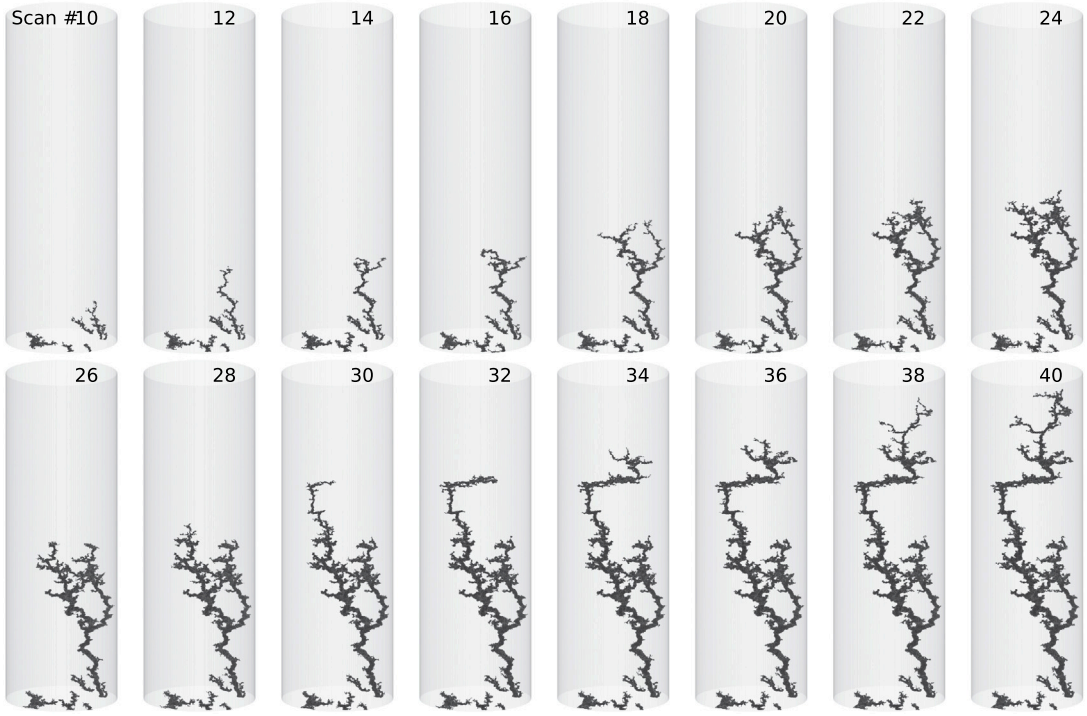

Fig. 1. Projections of 3D renders of a wormhole at different time instances showing the development of a wormhole in an acidized core of Pińczów Limestone. Rendered data is generated by subtracting a tomographic scan from the initial tomographic scan, and projections are generated in Tomviz. Diameter of plotted cylinders is 38.3 mm. Videos showing the full evolution of the wormhole in this experiment can be found in the Supplementary Material (Videos S1 and S2).

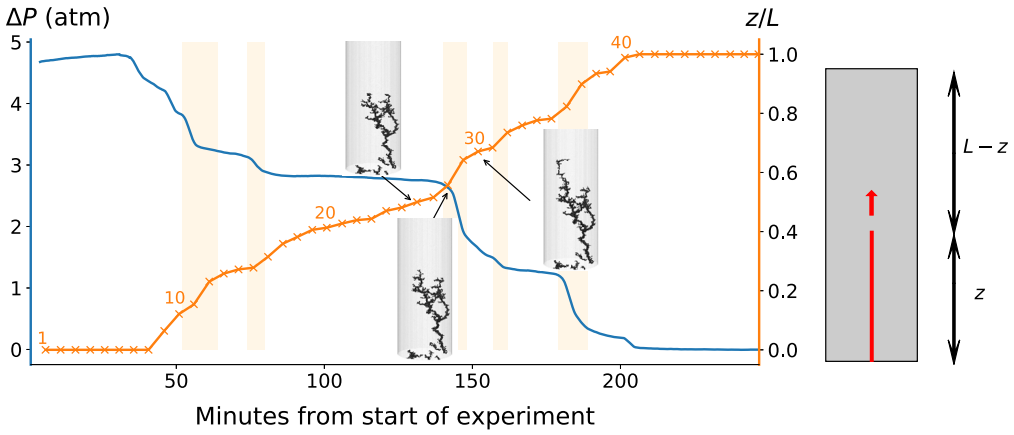

Fig. 2. (left) Experimental pressure drop in the Pińczów Limestone sample as a function of time (blue solid line) correlated with the wormhole tip position determined from the tomographic images (orange line with an X marking the end time of the scan). Orange numbers next to points indicate scan numbers corresponding to Fig. 1. (right) A simple model of propagating wormhole, in which it is assumed that the permeability of the system is controlled by the amount of material in front of the wormhole tip, $K(z) \sim (L-z)^{-1}$, where z is the extent of the wormhole and L is the total length of the system.

number of jumps, branchings, and sudden changes of direction. What is, however, more intriguing, is the apparent lack of correlation between the position of the tip and the changes of the permeability of the sample. The latter is measured by the pressure curve (Fig. 2) representing the pressure needed to pump fluid through the sample at a constant flow rate, at which the experiment is carried out. The pressure curve shows long plateaus interspersed with step-like pressure decreases.

Interpretation of this behavior is not straightforward; the simplest, but frequently used model of wormhole evolution argues that due to the high permeability of a wormhole, the pressure drop along its length is negligible (Daccord, 1987; Daccord et al., 1993; Hill et al., 1995; Li et al., 2019). Following this, and assuming that the rock in front of the wormhole tip is homogeneous, hydraulic resistance of the rock core should drop linearly with the length of the wormhole, $R \sim L-z$ where z is the length of the wormhole, and L is the total length of the system. An immediate consequence of this model is that pressure should decrease linearly with the advancement of a wormhole, $\frac{\Delta p}{\Delta p_0} = 1 - z/L$, with Δp_0 standing for an initial pressure drop through the sample. However, Fig. 2 shows that this is not the case for our system; during pressure plateaus the wormhole tip progresses noticeably with a nearly constant velocity. Such a behavior has been reported in only a few previous wormhole studies (Bazin et al., 1995; Izgec et al., 2010), with the response being attributed to vugs, where pressure drops are associated with wormhole/vug intersection (Izgec et al., 2010).

Pińczów Limestone, however, is not vuggy (Figarska-Warchoł and Stańczak, 2019), and as such we seek another explanation for this effect. We argue that such a behavior might be attributed to the presence of regions of very small porosity within the sample. Such

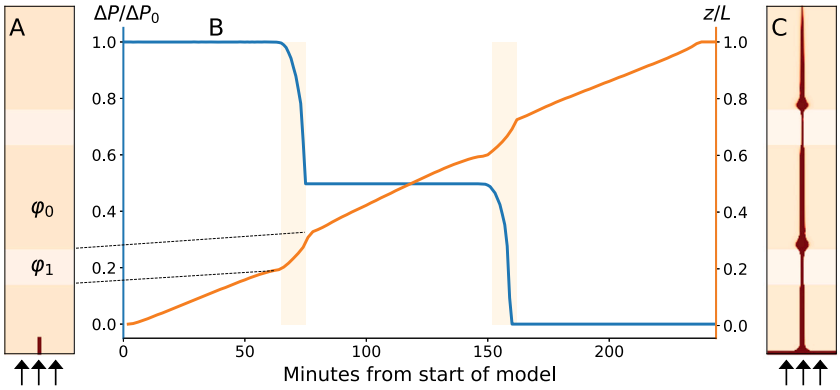

Fig. 3. A simple numerical model of wormhole growth in a layered medium. (A) The general setup; a rectangular system of porosity φ_0 with two layers of porosity φ_1, with $\varphi_1/\varphi_0 = 0.1$. (B) The pressure drop in the system (blue) and the tip position (orange) as a function of time. (C) The final dissolution pattern with shades of red marking porosity (fully dissolved regions correspond to dark red areas). Jumps in tip position and permeability correlate in time, with tip jumps correlating with regions of lower permeability.

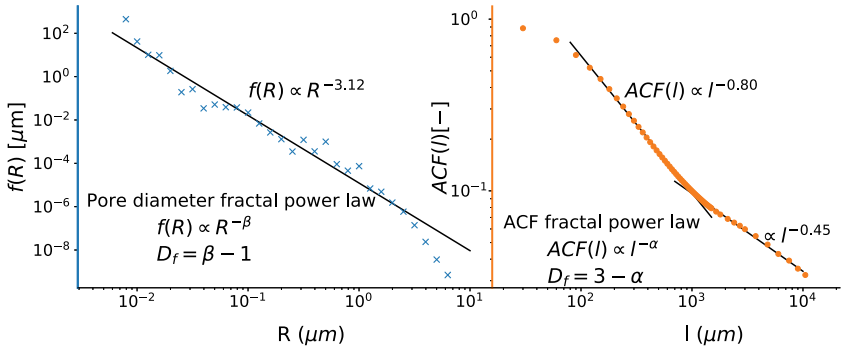

Fig. 4. Left: Pore radius distribution ($f(R)$) calculated from combined SANS and USANS results. Right: density–density auto-correlation function (ACF(l), where l is the linear scale) obtained from the tomographic images of the sample before acidization. Fractal dimension corresponding to $f(R)$ and ACF(l) both are ~ 2.1–2.2 in the scale range up to 1 mm. For scale lengths larger than 1 mm, ACF(l) decreases less steeply which indicates the presence of large-scale structures that control bulk geometry in this size range.

regions restrict the flow and effectively act as permeability barriers. Using analogy with the flow of electric current, the rock core would then resemble a circuit of resistors connected in series, with regions of small resistance interspersed with regions of very high resistance. If such a system was measured by an ohmmeter, the net resistance would be overwhelmed by high resistance regions. Only when the wormhole tip reaches high resistance regions and begins to etch its way through them, the permeability of the core changes in a noticeable manner.

3.2. Toy model

The mechanism of permeability variations can be demonstrated using a simple model of porous medium of porosity φ_0, which contains bands of much smaller porosity φ_1, marked by light yellow bands in Fig. 3A. We also introduced a small region of very high porosity near the inlet of the sample (marked by a red rectangle), to trigger wormhole formation at this point. We then let the system dissolve (using the numerical model described in A.5) and record the advancement of the tip and evolution of the pressure drop in time. Fig. 3B shows marked similarities with the analogous results for the experimental system, including long pressure plateaus during which the tip of the wormhole advances considerably. Interestingly, and somewhat surprisingly, the model calculations predict acceleration of the growth rate as the wormhole tip penetrates the impermeable layers in the model. The cause of this is that within a packed layer it is harder for the wormhole to broaden because there is more mineral matter to dissolve around the perimeter (Petrus and Szymczak, 2016). A thinner wormhole results in higher flow velocities within it, in turn leading to a larger propagation velocity of the wormhole tip.

3.3. Rock properties

Based on the 4D tomography results (Fig. 2) and theoretical considerations (Fig. 3), several questions arise: what is the real bulk pore-grain geometry of the sample? Are there any large-scale structures that can block flow paths? If so, do such structures correlate spatially with the wormhole tip position jumps?

To address these questions, an analysis of pore-grain structure was performed on length scales between 8 nm and 1 cm combining (ultra) small angle neutron scattering ((U)SANS, A.4) and image analysis of the tomography results obtained prior to the dissolution experiment (A.3, Fig. 4). Analysis of the smallest length scales used (U)SANS to determine the pore size distribution. Neutron scattering data shows an approximate power-law distribution (linear in log–log space) of pore radii, $f(R) \sim R^{-\beta}$, with $\beta = 3.12 \pm 0.2$ in the size range between 8 nm – 4 μm. This indicates an approximate self-similar pore structure with the fractal dimension $D_f = \beta - 1 \approx 2.12$ (Radlinski et al., 2004a; Anovitz and Cole, 2015). For $R > 4$ μm the deviation from the power law is likely due to multiple scattering (Ji et al., 2022) hence this range is excluded from the power law fit. To quantify the larger (> 30 μm) pore and grain architecture in the sample, we calculated the grayscale autocorrelation function on the tomographic data of the pre-dissolved sample, defined as

$$\mathrm{ACF}(\mathbf{l}) = \frac{\langle (g(\mathbf{r}+\mathbf{l}) - \mu)\,(g(\mathbf{r}) - \mu)\rangle_{\mathbf{r}}}{\langle (g(\mathbf{r}) - \mu)^2 \rangle_{\mathbf{r}}}, \tag{1}$$

where $g(\mathbf{r})$ is a grayscale value at point $\mathbf{r}$ within a sample and $\langle \dots \rangle_{\mathbf{r}}$ denotes averaging over $\mathbf{r}$. Finally, $\mu = \langle g(\mathbf{r}) \rangle_{\mathbf{r}}$ is the average grayscale

value. While computing ACF(**l**) we average over different orientations of the vector **l**, which gives a scalar dependent function ACF(l). Further details of the computation of the autocorrelation function are given in Appendix A.3.1.

The autocorrelation function approach has previously been used to characterize the pore space by first segmenting pores from grains (Katz and Thompson, 1985); in this work, however, we utilize the grayscale values of the images to capture both pores and the potential source of permeability barriers — the grains. Remarkably, for a wide range of radii (100 μm –1 mm), the autocorrelation function also shows a power-law behavior, $l^{-\alpha}$, with an exponent $\alpha = -0.8 \pm 0.01$ (Fig. 4). As it turns out, the power-law behavior of the autocorrelation function again implies fractal pore space geometry, however the link between the exponent and the fractal dimension is now different, $D_f = 3 - \alpha$ (Katz and Thompson, 1985). Remarkably, for our sample it again gives $D_f \approx 2.2$. Autocorrelation data from the experiment performed at Institut Laue-Langevin (Supplementary Material, Fig. 4) exhibit a similar power-law behavior with $D_f = 2.14$. These values are very close to the fractal dimension estimated form the neutron scattering data ($D_f = 2.12$). We can then conclude that combined U(SANS) and ACF data show a self-similar structure over a remarkably wide range of five orders of magnitude in pore sizes (8 nm–1 mm). However, as seen in Fig. 4, at R $\approx$ 1 mm there is a transition to a different scaling behavior, prevalent in the mm- and cm-range. The crossover to higher correlations indicate the presence of large structures, presumably fossil/grain assemblages on the scale of 1–10 mm. This is in full agreement with petrographic analyses of this rock type, which report horizontal laminae and recrystallized 1 mm thick zones parallel to the bedding (Figarska-Warchoł and Stańczak, 2019).

To determine if such large scale structures could be the permeability barriers postulated in our model (Fig. 3), we calculate the average grayscale intensity for successive slices perpendicular to the core (bedding) axis using a high resolution (30 μm voxels) tomographic image of the core prior to dissolution, taken outside of the core holder (full image processing information described in A.3). In X-ray tomography, image intensity represents the attenuation of matter to X-rays, which is proportional to its atomic number and density. Therefore, pixels of higher intensity correspond to regions with higher solid fraction or minerals with higher atomic numbers. For a rock dominated by one mineral (as is Pińczów Limestone) a higher average intensity corresponds therefore to a higher grain density (and thus, lower porosity). The data presented in Fig. 5C show quantifiable peaks, as determined by an automated peak detection algorithm (Virtanen et al., 2020), where average grayscale is higher than for the bulk of the rock. When wormhole tip displacement is juxtaposed with the average grayscale diagram, one notes that the wormhole propagation velocity increases in the peak regions, otherwise maintaining a steady velocity in the bulk of the rock (Fig. 5D). This supports our hypothesis that wormhole propagation rate is controlled by the permeability barriers within the sample. While a peak at $z/L \approx 0.1$ does not necessarily correlate to acceleration in the tip position, and the acceleration at $z/L \approx 0.7$ does not seem to be correlated with a peak, these two features are relatively narrow and thus the respective correlations might be harder to detect.

Naturally, projecting the grain content information on z axis (as performed in Fig. 5C) considerably smears out the data on the 3D configuration of pores, grains, and positions of the microcementation regions. As a result, the overall variations in the grain content remain relatively small, on the level of a few percent. This is much smaller than the ones used in the toy model of Fig. 3 when the porosity in the cemented regions was 10 times smaller than that in the bulk of the rock. Since both the pressure drops and the wormhole speedups recorded during the experiment are substantial (Fig. 2) we conclude that the wormhole tip does encounter local, highly cemented structures that it needs either to navigate around, or dissolve its way through. The coarse projection of Fig. 5C succeeds in picking up the most extended of these regions but - as already mentioned - misses a thinner one at $z \approx 0.7$, as marked in Fig. 2.

Finally, to investigate what rock textures correspond to the regions of permeability barriers, we analyze thin sections taken from another core of the same rock (eight perpendicular and one parallel to the core axis, which is perpendicular to the bedding) at varying positions. Petrography of Pińczów limestone is briefly summarized in Section 2.1. Fig. 6 shows two representative images of the thin sections in crossed-polar light (XPL) to highlight mineralogical and textural differences. Thin section A is taken from the bulk region (corresponding to relatively low grayscale pixel intensity); it contains abundant calcite mud (brown regions), interspersed with fossil grains, with no well-connected large-scale structures. Between and within fossil grains are numerous, visible pores. In contrast, thin section B, corresponding to what we hypothesize to be a permeability barrier, contains a larger amount of fossils, less mud and pores, and an abundance of microcrystalline spar indicated by gray and high birefringence colors. Crystalline spar and grains in this case are of similar appearance/mineralogy, have low porosity, and make up larger, cemented together, structures. The grayscale autocorrelation function was calculated from two-dimensional plane-polarized light (PPL) images of the thin sections, as a single material appears on such scans as the same grayscale value, unlike XPL. The ACF shows that both thin sections have similar fractal dimensions for linear scales $\sim$ 30 μm $\leq l \leq$ 0.5 mm with $D_f \approx 2.19 \pm 0.03$ for thin section A, and $D_f \approx 2.15 \pm 0.03$ for thin section B. For scales $\geq$ 0.5 mm the fractal dimension increases for thin section B to $D_f \approx 2.39 \pm 0.12$, with larger features (i.e., the cemented spar and grains) being better correlated, whereas D_f remains unchanged for all feature sizes for thin section A. This confirms that the volume-averaged transition from $D_f \approx 2.1$–2.2 to $D_f \approx 2.55$, observed in the grayscale correlation function for the original sample (Fig. 4) is associated with microstructural features of the low-porosity regions. Peaks in the mean grayscale intensity can thus be interpreted as the result of low porosity layers dominated by grains cemented by calcite spar, which act as permeability barriers. Full data on all thin sections is presented in Supplementary Material, Sec. 2.

4. Discussion and conclusions

The data presented in this paper demonstrate the benefit of high temporal and spatial resolution tomography in reactive flow studies. In particular, our results reveal that growth of wormholes in a real limestone rock can be more complex than simple proportionality of the driving pressure and tip displacement predicted by a typical model which assumes micro-structural homogeneity (Daccord, 1987; Daccord and Lenormand, 1987; Hill et al., 1995; Li et al., 2019). In our samples, we observe temporal plateaus of little pressure change, alternated with larger drops in pressure which correlate well with the predictions of a conceptual model that assumes a layered porosity distribution. Our numerical results reproduce the general character of the observed pressure curve (Fig. 3), and predict jumps in wormhole tip position. The high temporal resolution of the 4D tomography technique used here enabled the capture of wormhole growth characteristics corresponding to temporal variation of the driving pressure. This made it possible to test the permeability barrier model and show that tip velocity increases as the wormhole penetrates the barrier. We note that the finite duration of tomographic scans ($\sim$ 5 min) results in temporal averaging of tip velocities, which may obscure the presence of relatively narrow high density layers (as at $z/L \sim 0.1$ in Fig. 5). This demonstrates that 4D tomography is a trade off in spatial versus temporal resolution, as well as the volume of data. If one wanted to capture very fine tip advancement in small layers, it is advised to observe the time scales at which the pressure jumps occur in samples of a particular kind and tune scanning time to allow for multiple scans over that time scale. Additionally, the time scales can be adjusted by decreasing

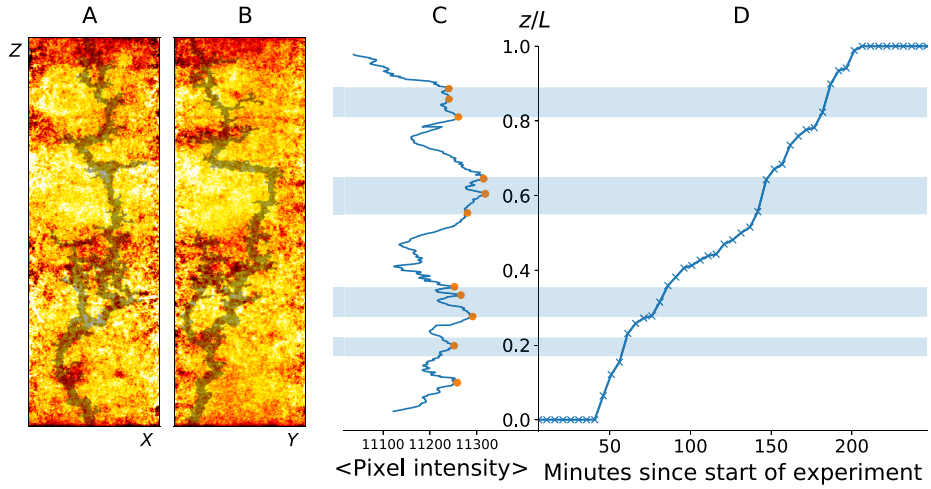

Fig. 5. Average grayscale pixel intensity (C) through slices perpendicular to the core axis spatially-correlated to tip position, z/L (L = 115 mm), plotted versus time (D). A and B show the median grayscale value in the X and Y axis, respectively, with reds corresponding to regions with less intensity (more porous) and yellow/white corresponding to regions with more intensity (grains/crystalline calcite). Median values are derived from the high resolution, 30 μm initial image, and are overlaid with the final wormhole geometry projected in the same axis. Large propagation velocities are associated with high average grayscale pixel intensity, a proxy for solid content. As the wormhole dissolves its way through the packed regions it remains a single channel with minimal branching, with branching and lateral movement occurring before entering the cemented regions.

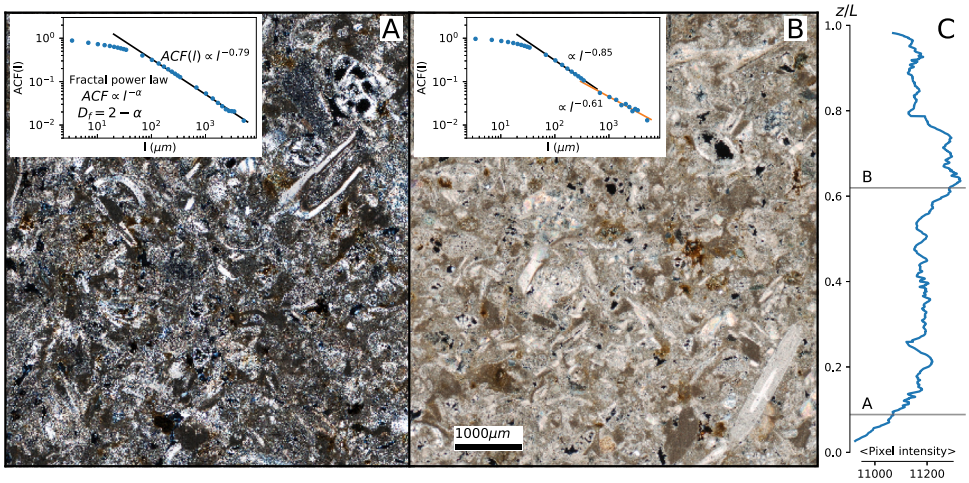

Fig. 6. Representative cross-polarized light (XPL) images of thin sections (A and B) of a Pińczów Limestone core, taken perpendicular to its axis. Thin section A contains abundant calcite mud (brown), interspersed with fossil grains (lighter colors) and open pores at all scales, while thin section B contains mud and pores at small scales, a larger amount of large fossils, and a matrix dominated by calcite spar. Spar and grain in thin section B create a large scale structure of low porosity. Insets in A and B are plots of the grayscale autocorrelation function computed using plane-polar light (PPL) images. Prior to sectioning, the core was scanned with tomography, and the average grayscale value for each slice perpendicular to the core and bedding axis was calculated (C). Locations of where thin sections were taken are labeled with A and B.

acid concentration, however, this increases experimental time and the amount of image data collected.

The micro-geometric characteristics of Pińczów Limestone sample, obtained from the results of SANS and USANS, high resolution tomography, and thin section polarized microscopy measurements, provided key insights allowing the analysis and interpretation of the kinetics of wormhole propagation through the rock. Each of these methods revealed a fractal geometry of the pore-rock matrix interface characterized by a surface fractal dimension $D_f \approx 2.1$–2.2, jointly extending across many orders of magnitude, from nanometers to 0.5–1 mm, with a switch-over to a larger fractal dimension ($D_f \approx 2.55$) at scales corresponding to the average fossil grain size in the rock (≈ 0.5–1 mm). The observed spatial correlation of wormhole tip propagation velocity with average grayscale intensity indicates that regions which contain these large structures act as barriers to reactive flow. As in the presented numerical model, tip velocity increases as the wormhole penetrates these barriers.

The speedup of the wormhole tip as it goes through the cemented regions has been observed before (Petrus and Szymczak, 2016) but only a qualitative explanation of this phenomenon was given: since there is a larger amount of material to dissolve to broaden the wormhole, its radius remains relatively small. Due to the conservation of mass, a smaller radius implies larger flow velocities within the wormhole, and hence also faster propagation speeds of its tip. This qualitative picture is in agreement with the results of numerical simulations (Petrus and Szymczak, 2016), though an explicit formula linking the wormhole radius with the physical and chemical properties of the surrounding rock is lacking. Such a formula would have allowed for estimating the porosity contrast between the cementation regions and the bulk of the sample based on the tip advancement data, which would be an important complement to the present study.

Another complementary approach would be to analyze the evolving flow field associated with these wormholing patterns. As shown in Petrus and Szymczak (2016) the movement of the tip of the wormhole into and out of the packed layers is associated with significant

changes in the flow patterns. As the tip of the wormhole enters a cemented layer, the flow near the tip becomes strongly focused, with diminished transverse components. On the other hand, as the wormhole emerges from the layer, the flow spreads out from the wormhole tip, analogously to the flow created by the point source at the wall. These effects should be detectable with the flow imaging techniques such as NMR (Muljadi et al., 2018; Oliveira et al., 2021; Elsayed et al., 2023).

Finally, let us note that cemented regions in the core can have yet another impact on the wormhole advancement, as the wormhole might try to avoid the low permeability, crystalline portions by progressing laterally. In essence, the wormhole searches for an easiest-to-dissolve pathway that would lead it through the barrier. This is a three-dimensional effect, not possible to represent in terms of our 1D toy model, since in the latter there is no possibility of bypassing the packed layers. In our experiment, this happens between frames 13–15, 30–31 and 33–35, i.e., just before the encounter with the cemented region. In the first and third case (13–15 and 33–35) this lateral movement is also accompanied by an intense branching of the wormhole, as if it is probing different ways through the obstacle before finding the most effective one (see e.g. frame 34 in Fig. 1). The quantification of the lateral movement of the wormhole is provided by Fig. 5 in the Supplementary Material which compares the axial movement of the wormhole tip (along z) with the total movement. As observed, in the regions where $z(t)$ plot is almost flat (no axial advancement), there is still a noticeable advancement in the absolute length of the wormhole, $L_W(t)$. Note that the vertical scale on the two plots are different due to the large tortuosity of the wormhole (its absolute length is about two times larger than its extent in z direction, thus the real slopes of the $L_W(t)$ line are about twice larger than the $z(t)$.

As we already mentioned, there are limited other wormhole studies reporting a similar type of pressure curve with plateaus and jumps, attributed to vugs (Izgec et al., 2010). We do not see an abundance of vugs in Pińczów Limestone indicated in either thin sections or tomographic images. Furthermore, tomographic images of areas containing vugs would show a smaller than average pixel intensity, therefore the wormhole tip velocity jumps would then be correlated to troughs rather than peaks of pixel intensity.

Despite the differences highlighted above, both models converge in their emphasis on the importance of rock heterogeneity; both vugs and permeability barriers are possible structural heterogeneities in limestone, whereas most wormhole propagation models assume full homogeneity. Consequently, the rate of the wormhole tip propagation extracted from 4D tomography can be used to detect and analyze the micro-scale heterogeneities embedded in the rock. Since the growth is driven by an imposed flow, the dynamics of the wormhole is sensitive to the local connectivity of competing reactive flow paths, making it possible to detect micro-laminations and structural discontinuities which are hard to identify with other methods.

Finally, the data from 4D tomography provides a perfect testing ground for numerical simulation of reactive flow in porous rocks (Molins et al., 2020; Ladd and Szymczak, 2021), particularly multi-scale approaches (Molins et al., 2012; Yang et al., 2013; Hao et al., 2013; Soulaine et al., 2017; Ferreira et al., 2020; Agrawal et al., 2020; Noiriel et al., 2021) which attempt to bridge the scales between the pore-scale processes and formation of large-scale patterns. Wormholing analyzed in this study is a striking example of such a process — flow evolution in the sample results from the coupling between the large-scale properties of a wormhole as a whole with local interactions of its tip with the small-scale heterogeneities in the rock. An in-depth understanding of the coupling between these processes is crucial for the prediction of wormhole propagation speed and permeability evolution at the reservoir scale for the systems where wormholing is of a practical importance, such as controlling contaminant migration or preventing CO_2 leakage during geological carbon sequestration.

CRediT authorship contribution statement

Max P. Cooper: Designed and conducted the experiments, prepared cores, performed data analysis and curation, developed Python scripts, and co-wrote the manuscript including production of figures. **Rishabh P. Sharma:** Helped conduct experiments, write Python scripts, and perform data analysis. **Silvana Magni:** Helped with core preparation and conducting experiments. **Tomasz P. Blach:** Co-designed the initial experimental apparatus and helped conduct acidization experiments, acquired beamtime and prepared samples for (U)SANS measurements and conducted those measurements. **Andrzej P. Radlinski:** Designed the experimental apparatus and initial protocol, helped acquire funding and materials, designed the lab at University of Warsaw, helped conduct the acidization experiments, acquired beamtime and prepared samples for (U)SANS measurements, conducted those measurements and performed data analysis, wrote (U)SANS methods for the initial manuscript, and greatly helped in establishing relationships with INiG-PIB and ILL. **Katarzyna Drabik:** Acquired and reconstructed tomography data at INiG-PIB. **Alessandro Tengattini:** Helped run experiments, set up data acquisition and reconstructed tomography data on the NeXT instrument, and edited the initial manuscript. **Piotr Szymczak:** Designed experiments and helped conduct them, acquired funding and materials, supervised the group, performed numerical simulations, co-wrote the manuscript including production of figures, and noticed the unique behavior in experiments that led to this article.

Declaration of competing interest

The authors declare that they have no known competing financial interests or personal relationships that could have appeared to influence the work reported in this paper.

Data availability

Codes and raw as well as processed data are available at https://doi.org/10.5281/zenodo.7558135. Raw tomographic data are available at https://doi.org/10.5281/zenodo.7683242.

Acknowledgments

This work was supported by the National Science Center (Poland) under research Grant No. 2016/21/B/ST3/01373. We acknowledge the Institut Laue-Langevin for the allocated beam time on D11, S18 and NeXT. We would like to thank the instrument scientists for the (U)SANS instruments at Institut Laue Lanvgevin, Ralf Schweins (SANS, instrument D11) and Hartmut Lemmel (USANS, instrument S18), Phung N.H. Vu for aiding in (U)SANS experiments, and Marek Dohnalik for aiding with tomography at INiG-PIB. Additionally, we would like to thank Anna Poszytek for high resolution imaging of the thin sections, Eric Cooper for creating thin section masks, and Jacek Łata of Marmur-Płytki, Pińczów, Poland for the donation of a Pińczów Limestone block used in this study. Finally, we thank Mariusz Białecki for his valuable suggestions for figure improvements.

Appendix A. Extended methods

A.1. Rock preparation

A.1.1. Cores

Cores of Pińczów Limestone were prepared using a coring bit attached to a drill press designed for rock cutting. The coring bit used in the experiment presented here produces samples with a diameter of 38.3 mm, and lengths ~150 mm, taken perpendicular to the bedding direction. Cores are then further cut to length with a diamond bladed trim saw. The typical length of cores prepared (and the length in the experiment presented in the main text) is 115 mm.

A.1.2. SANS and USANS

The Pińczów Limestone sample measured by SANS and USANS was in the form of nearly-monodisperse coarse grains, gently crushed by hand and sieved to the fraction 0.355 mm < D < 0.425 mm, where D is grain diameter. The size of the grains is optimized in such a way that scattering measurements provide information averaged over the orientation of the grains. This sample was confined in an aluminum container with an internal volume of 0.123 cm^3 and an internal thickness of 1 mm; the volume filling factor determined by weighing was 0.589. Mineralogically, the sample was nearly pure calcite with matrix skeleton density of 2.71 g/cm^3; the nominal porosity of the measured Pińczów Limestone sample was ~30%.

A.2. Time-lapse dissolution-tomography experiments

In this article we present an experiment with a high temporal resolution of five minutes per scan over five hours during active wormhole formation. This experiment was performed at the Oil and Gas Institute - National Research Institute (INiG-PIB) in Krakow, Poland. The experimental apparatus setup is that of a classic core flooding experiment, *e.g.,* Fredd and Fogler (1998). Cylindrical cores, along with ceramic disks (Soilmoisture 0.5 Bar High Flow plates, machined to 38.3 mm diameter) to ensure uniform flow, are placed inside a Viton sleeve and mounted in a high pressure core holder (Phoenix Instruments, with the maximal core diameter 1.5 inch [38.3 mm] and length 5.5 inches [140 mm]). Core lengths are adjustable by filling the remaining length of the core holder with cylindrical PTFE spacers. Confinement pressure was supplied by an external source of pressurized nitrogen. Flow rate of water/HCl solution (0.25M for the presented experiment) was controlled using a computer controlled high pressure dual-piston pump (Vindum Engineering, Inc. VP-3K) and a back pressure regulator (Equilibar U3L0), used to prevent phase separation of CO_2 generated during dissolution. A control and monitoring system of valves and a pressure transducer (Keller series PD-39X) enable monitoring the pressure drop across the cell. The appropriate back pressure was adjusted to acid concentration using Henry's law (Sander, 2015), and the confinement pressure was set to the sum of the back pressure and the initial pressure drop across the sample, plus a 10% overhead. All fluids were degassed under dynamic vacuum prior to an experiment, and all fluid lines as well as the core were pre-saturated with deionized water to ensure single phase flow through the entire system. During an experiment the pressure is logged at an interval of 10 s, we also log the starting and stopping time for each scan. For visualization quality a rolling average over 20 pressure samples is applied for Fig. 2.

To obtain the time series scans the cell is placed in a tomograph. The tomograph at INiG is a model RXCT GeoTek Ltd. machine, which is designed specifically to scan long cores in a horizontal orientation, with the X-ray source (Thermo Kevex Microfocus, 45 to 130 kV, 4 to 65 W) and detector (Varian PAXScan 2520DX, 1920 × 1536 16-bit pixels) rotating around the core. This machine can select from a variety of voxel resolutions 30–350 μm, depending on the distance between source and detector, and pixel binning on the detector. In normal operation, cores are held in a plexiglass tube that is attached to motorized manipulator arms capable of repeatable positioning, as to allow cores longer than the field of view to be scanned. To scan actively dissolving cores, the fluid and confining gas lines are routed into one of the arm housings through the cable ingress hole, and the core holder is attached to the arms with machined adapters.

To determine the optimal acquisition settings using the tomograph at INiG-PIB, an imaging experiment was performed prior to the dissolution experiment. Three static scans were performed with a partially dissolved core within the core holder at 42 μm, 84.5 μm, and 169 μm voxel resolution, with decreasing magnification obtained by adjusting the source to detector distance (42 to 84.5 μm), or increasing the binning factor (2 × 2 binning of 84.5 μm to produce 169 μm voxels), which tightens the grayscale distribution (Supplementary Material, Fig. 15) and shifts threshold values for pores (Supplementary Material, Table 2). As voxel size increases, the acquisition time decreases, as fewer images are taken per scan. These scans take 10, 6, and 5 min, respectively. This includes the tomography itself, plus the rotation of the detector/source back to the initial position. As the core is longer than the field of view, the arm moves the entire core holder and imaging/rotation is repeated for the upper half of the core. For example, for acquisition at 169 μm, the first tomography lasts 60 s, followed by a gap consisting of repositioning the core holder and rotation back to the 0-degree position (70 s), the second tomography (60 s), and a period resetting to the initial configuration and processing (105 s). After reconstruction, these two separate image stacks are joined together. Due to this stacking, the upper portion of the core is not time-synchronous with the lower half; however, the time elapsed between acquisitions of a given half is equal between captures.

This imaging experiment reveals that there is a trade-off between the image acquisition time (temporal resolution) and spatial resolution; however, the measurement of interest, the tip position versus time, can still be carried out with an acceptable accuracy (Supplementary Material, Sec. 3). Other parameters, such as wormhole volume, are not as robust to changes in voxel size due to tightening of the grayscale distribution and additional noise, as seen in Table 2 and Fig. 15 in the Supplementary Material. Since the wormhole growth is highly dynamic, we have decided to maximize the temporal resolution and, consequently, the five minute duration, 169 μm voxel resolution scans are used. In addition to the time-lapse scans, high resolution (30 μm) scans of both the initial and final core outside of the dissolution cell are taken.

An additional pressure log of a benchtop experiment, as well as another experiment that was scanned with 4D tomography are presented in Supplementary Material, Sec. 1. This 4D experiment was performed on the combined neutron and X-ray tomography instrument (NeXT) at Institut-Laue Langevin, Grenoble, France (Tengattini et al., 2020). Here the X-ray source (Hamamatsu L12161-07) and detector (Varex PaxScan 2530HE, 1792 × 2176 16-bit pixels) are stationary, with rotation provided by a motorized, high accuracy table, to which the cell holder is attached in a vertical orientation.

A.3. Image processing

Processing of all tomographic and microscopy images were performed in FIJI/ImageJ and a series of Python scripts utilizing the NumPy (Harris et al., 2020), SciPy (Virtanen et al., 2020), and scikit-image (Van der Walt et al., 2014) libraries.

A.3.1. Static tomography analysis

Several analyses of the pore and grain geometry on the initial, high resolution tomography were performed. To prepare the reconstructed tomography for automated analyses, first the 3D stack of (tiff formatted) images were cropped to a size that included the entire core but minimal surrounding areas. To remove excess surrounding data (essentially empty space and the plexiglass tube the core was placed in), a mask was prepared in ImageJ by first setting a grayscale threshold, then using the Analyze Particles feature with a large (10^5) minimum size. This gives a mask where voxels within the core have a value of 1, and all other voxels are 0. Multiplication by this mask results in a 3D image stack of the core surrounded by voxels with a grayscale value of zero. Before measuring the grayscale autocorrelation function (ACF(l)) the data is further corrected to remove any beam hardening artefacts by another cropping step to leave just the central part of the core, which is less affected by this artefact. As beam hardening affects each slice of the core equally, the full core is used in average intensity measurements.

The grayscale autocorrelation function (ACF(l)), which is essentially the density–density autocorrelation function, was computed for a variety of lengths, l, between 30 μm and 1 cm on the initial, high resolution scan. Computation of ACF(l) was performed in a Python

script, with the main computation step performed in Cython. Firstly, the average grayscale over the number of non-zero (non-masked) voxels is calculated and subtracted from the 3D image in the masked region. The main computation step then loops over each voxel, adding the voxel grayscale values I distance away in the ±x, ±y, and ±z directions, unless such a voxel lies outside the image boundary. ACF(l) is then computed using Eq. (1), which is fully described in the main text. Curves were fit to this data with linear regression in SciPy to determine fractal dimensions.

To calculate average intensities in successive x-y slices perpendicular to the core axis (z-axis) a Python script was used that sums every grayscale value in a slice and divides by the number of non-zero (non-masked) pixels in that slice. To determine peaks of high intensity in the profile automatically, a peak detection algorithm is employed, utilizing the signal library within SciPy (Virtanen et al., 2020). Prior to peak detection, a Gaussian filter with a standard deviation of 50 and a size of 15 is convolved with the average intensity array to reduce the number of lesser, local maxima. For Fig. 5 of the main text, peak finding parameters are a height greater than the average intensity, at least 80 slices apart, and a peak prominence of 5.

In addition to the analysis of the static initial scan, wormhole extraction from static final scans of a partially dissolved core was performed during the imaging experiment used to determine acquisition parameters. To extract the wormhole a grayscale threshold, dependent on voxel resolution (Supplementary Material, Table 2), was applied to the tomographic image in Python, resulting in a binary image. Following binarization, the wormhole was isolated from pores by choosing a seed point within the wormhole, and applying an algorithm that saves pixels of the same grayscale value (or within a threshold) that are connected to that seed point, termed the *flood fill* algorithm in scikit-image (Van der Walt et al., 2014).

A.3.2. Dynamic tomography analysis

The 4D tomographic data was processed by a series of Python scripts to extract wormhole geometry for visualization and automatic tip position measurement. After cropping, each scan was subtracted from the initial scan within the core holder (of same resolution as other scans in the 4D sequence) in order to isolate the areas that had transitioned from grain to pore. For high contrast visualization purposes in Video S1, Fig. 1, and Fig. 2, wormholes were extracted using the method described for the imaging experiment. As there are multiple initial wormholes, multiple seed points were chosen manually and the flood fill algorithm was applied to each time series image.

For automatic tip position measurement the subtracted images were skeletonized to obtain a volume where each wormhole branch is indicated by a single pixel per slice. These images allow, combined with filtering, a straightforward identification of tip position. Prior to skeletonization, a median filter with a 3 × 3 × 3 window is applied, followed by a binary threshold where grayscale intensities greater than 500 are represented by a True value, and a hole filling algorithm is applied in SciPy (Virtanen et al., 2020). The image is then skeletonized using the 3D skeletonize function in scikit-image (Van der Walt et al., 2014).

To remove any remaining noise, a 9 × 9 × 9 kernel of all ones is convolved with the skeletonized image to count the number of skeleton voxels surrounding a particular voxel. Skeleton voxels with fewer than 5 neighbors are then removed from the selection to minimize the effect of randomness deriving from the unavoidable noise of the high speed tomographic imaging and subsequent treatments. The value of 5 derives from the fact that a wormhole will have either 4 voxels ahead of the center voxel (at the "root" of the wormhole), 4 voxels behind the center voxel (at the tip), or to any side in a 9 × 9 × 9 window. A second pass is performed with a 3 × 3 × 3 ones kernel to remove single voxel skeletons. Finally, isolated skeletons are removed from the stack if there is no skeleton present 5 slices behind in the z direction.

Following filtering, the presence of skeleton was evaluated by summing pixels in each x-y slice. The largest non-zero index of this count array is taken to be the tip position.

For the 4D experiment presented in Sec. 1 of the Supplementary Material the same procedure is used, however with a grayscale threshold value of 15 000.

A.3.3. Thin section image analysis

Thin sections were imaged in crossed-polar and plane polar light (XPL and PPL) on a Nikon ECLIPSE LV100N POL polarized light microscope with a motorized stage (Märzhäuser Wetzlar) and Nikon DS-5Mc camera to image the entire thin section, resulting in color (RGB) tiff images with 8-bits per color channel. Thin sections at 10, 20, 30, and 35 mm were imaged at 4x magnification, resulting in a pixel size of 1.7 μm, while 50, 60, 70 and 80 mm sections were imaged at 2x magnification (3.4 μm per pixel). Thin sections were visually inspected for their mineralogy and matrix/grain content. Images were converted to 8-bit grayscale in FIJI/ImageJ and masks were created in Adobe PhotoShop for ACF(l) computation by creating a new layer, painting pixels that are not within the rock portion of the image white, selecting the white portion with the wand tool to fill it with black (giving a value of 0 where there is no thin section), then inverting the selection and filling with white (value of 1 where the thin section is present). Grayscale autocorrelation was computed using the same code as in tomographic images, however, only in the ±x and ±y directions.

A.4. SANS and USANS measurements

Small-angle neutron scattering measurements were conducted using SANS instrument D11 (Lindner and Schweins, 2010) and USANS instrument S18 (Hainbuchner et al., 2000) at the Institut Laue Langevin, Grenoble. Data were collected in the Q-range $2.99{\cdot}10^{-5}$Å^{-1}<Q< $1{\cdot}10^{-3}$ Å^{-1} for USANS and $2{\cdot}10^{-3}$Å^{-1} < Q < $3.13{\cdot}10^{-2}$Å^{-1} for SANS; i.e., in the combined Q-range of $2.99{\cdot}10^{-5}$Å^{-1} < Q < $3.13{\cdot}10^{-2}$Å^{-1}, where $Q = (4\pi/\lambda)(sin\theta)$ is the modulus of the scattering vector, 2θ is the scattering angle and λ is the neutron wavelength. Acquired raw data were processed using data reduction protocols described in the literature (e.g., Gu and Mildner (2018), Radlinski (2006)) to obtain the pore size distribution expressed as a histogram, using the Polydisperse Spheres (PDSP) model implemented in PRINSAS software (Hinde, 2004; Radlinski et al., 2004b).

Such a Q-range of scattering vectors corresponds to the range of pore sizes, $D = 5/Q$ from ~16 nm to ~17 μm (Radlinski et al., 2000). Scattering length density of $4.69{\times}10^{10}$ cm^{-2} was calculated from the mineral composition (pure $CaCO_3$) and physical density of the rock matrix (2.71 g/cm^3).

A.5. Numerical model of rock acidization

The numerical model of rock acidization is based on the coupled equation for flow, reactant transport, and porosity evolution at the Darcy scale (Ladd and Szymczak, 2021). The Darcy equation for the steady-state flow is solved first, followed by an advection–diffusion–reaction equation for reactant transport, assuming one-component, linear reaction kinetics. Finally, we increase the porosity in proportion to the reactive flux in a given point of the sample. These equations are solved using the finite-difference *porous* package, developed by Upadhyay et al. (2015), which utilizes finite-difference methods with a parallel multigrid linear solver *Hypre* (Falgout and Yang, 2002). The details of the particular implementation of this model used in the present study can be found in Upadhyay et al. (2015). The simulations presented in Fig. 3 are run on a regular 200 × 1000 mesh, with the initial porosity equal to 0.3 throughout the sample except in two horizontal strips (Fig. 3) where it is equal to 0.03. The permeability was assumed to depend on porosity as $K(\varphi) \sim \varphi^3$, which corresponds to the Carman–Kozeny law with a constant surface area (Szymczak and Ladd, 2014). The linear reaction rate was assumed, $R = kcs$, with a constant reactive surface area (s).

Appendix B. Supplementary data

Supplementary material related to this article can be found online at https://doi.org/10.1016/j.advwatres.2023.104407. It contains two videos of wormhole development and pdf with additional experimental data.

References

Agrawal, P., Raoof, A., Iliev, O., Wolthers, M., 2020. Evolution of pore-shape and its impact on pore conductivity during CO2 injection in calcite: Single pore simulations and microfluidic experiments. Adv. Water Resour. 136, 103480.

Aharonov, E., Whitehead, J., Kelemen, P., Spiegelman, M., 1995. Channeling instability of upwelling melt in the mantle. J. Geophys. Res. 100, 433–455.

Al-Khulaifi, Y., Lin, Q., Blunt, M.J., Bijeljic, B., 2019. Pore-scale dissolution by CO_2 saturated brine in a multimineral carbonate at reservoir conditions: Impact of physical and chemical heterogeneity. Water Resour. Res. 55 (4), 3171–3193.

Anovitz, L.M., Cole, D.R., 2015. Characterization and analysis of porosity and pore structures. Rev. Mineral. Geochem. 80 (1), 61–164.

Bazin, B., Bieber, M., Roque, C., Bouteca, M., et al., 1996. Improvement in the characterization of the acid wormholing by in situ X-ray CT visualizations. In: SPE Formation Damage Control Symposium, Lafayette, Louisiana, 1996, Paper Number: SPE-31073-MS. Society of Petroleum Engineers.

Bazin, B., Roque, C., Bouteca, M., 1995. A laboratory evaluation of acid propagation in relation to acid fracturing: Results and interpretation. In: SPE European Formation Damage Conference, the Hague, Netherlands, 1995, Paper Number: SPE-30085-MS. Society of Petroleum Engineers.

Buijse, M., 1997. Mechanisms of wormholing in carbonate acidizing. In: International Symposium on Oilfield Chemistry, Houston, Texas, 1997, Paper Number: SPE-37283-MS. Society of Petroleum Engineers.

Cohen, C., Ding, D., Quintard, M., Bazin, B., 2008. From pore scale to wellbore scale: Impact of geometry on wormhole growth in carbonate acidization. Chem. Eng. Sci. 63, 3088–3099.

Daccord, G., 1987. Chemical dissolution of a porous medium by a reactive fluid. Phys. Rev. Lett. 58 (5), 479–482.

Daccord, G., Lenormand, R., 1987. Fractal patterns from chemical dissolution. Nature 325, 41–43.

Daccord, G., Lenormand, R., Liétard, O., 1993. Chemical dissolution of a porous medium by a reactive fluid - I. Model for the wormholing phenomenon. Chem. Eng. Sci. 48, 169–178.

Daccord, G., Touboul, E., Lenormand, R., 1989. Chemical dissolution of a porous medium: limits of the fractal behaviour. Geoderma 44 (2–3), 159–165.

Daines, M.J., Kohlstedt, D.L., 1994. The transition from porous to channelized flow due to melt/rock reaction during melt migration. Geophys. Res. Lett. 21, 145–148.

Detwiler, R.L., Glass, R.J., Bourcier, W.L., 2003. Experimental observations of fracture dissolution: The role of Péclet number in evolving aperture variability. Geophys. Res. Lett. 30, 1648.

Elkhoury, J.E., Ameli, P., Detwiler, R.L., 2013. Dissolution and deformation in fractured carbonates caused by flow of CO_2-rich brine under reservoir conditions. Int. J. Greenhouse Gas Control 16, S203–S215.

Elsayed, M., BinGhanim, A., Aljawad, M.S., El-Husseiny, A., Al-Abdrabalnabi, R., Mahmoud, M., 2023. Quantifying acid diversion efficiency through NMR tortuosity measurements. J. Pet. Explor. Prod. Technol. 13, 917–927.

Falgout, R.D., Yang, U.M., 2002. Hypre: a library of high performance preconditioners. In: Computational Science - ICCS 2002, International Conference, Amsterdam, the Netherlands, April 21-24, 2002. Proceedings, Part III. pp. 632–641.

Ferreira, L.d.P., Surmas, R., Tonietto, S.N., da Silva, M.A.P., Peçanha, R.P., 2020. Modeling reactive flow on carbonates with realistic porosity and permeability fields. Adv. Water Resour. 139, 103564.

Figarska-Warchoł, B., Stańczak, G., 2019. The effect of petrographic characteristics on the physical and mechanical properties of currently exploited Pińczów limestones–a type of Leitha Limestone (Carpathian Foredeep, southern Poland). Min. Resour. Manag. 35, 59–98.

Fleury, V., Gouyet, J.-F., Léonetti, M., 2013. Branching in Nature: Dynamics and Morphogenesis of Branching Structures, from Cell to River Networks. Springer Science & Business Media.

Fredd, C.N., Fogler, H.S., 1998. Influence of transport and reaction on wormhole formation in porous media. AIChE J. 44, 1933–1949.

Garcia-Rios, M., Cama, J., Luquot, L., Soler, J.M., 2014. Interaction between CO_2-rich sulfate solutions and carbonate reservoir rocks from atmospheric to supercritical CO_2 conditions: Experiments and modeling. Chem. Geol. 383, 107–122.

Garcia-Rios, M., Luquot, L., Soler, J.M., Cama, J., 2015. Influence of the flow rate on dissolution and precipitation features during percolation of CO_2-rich sulfate solutions through fractured limestone samples. Chem. Geol. 414, 95–108.

Golfier, F., Zarcone, C., Bazin, B., Lenormand, R., Lasseux, D., Quintard, M., 2002. On the ability of a Darcy-scale model to capture wormhole formation during the dissolution of a porous medium. J. Fluid Mech. 457, 213–254.

Gu, X., Mildner, D.F., 2018. Determination of porosity in anisotropic fractal systems by neutron scattering. J. Appl. Crystallogr. 51 (1), 175–184.

Hainbuchner, M., Villa, M., Kroupa, G., Brückner, G., Baron, M., Amenitsch, H., Seidl, E., Rauch, H., 2000. The new high resolution ultra small-angle neutron scattering instrument at the High Flux Reactor in Grenoble. J. Appl. Crystallogr. 33 (3), 851–854.

Hao, Y., Smith, M., Sholokhova, Y., Carroll, S., 2013. CO_2-Induced dissolution of low permeability carbonates. Part II : Numerical modeling of experiments. Adv. Water Res. 62, 388–408.

Harris, C.R., Millman, K.J., van der Walt, S.J., Gommers, R., Virtanen, P., Cournapeau, D., Wieser, E., Taylor, J., Berg, S., Smith, N.J., Kern, R., Picus, M., Hoyer, S., van Kerkwijk, M.H., Brett, M., Haldane, A., del Río, J.F., Wiebe, M., Peterson, P., Gérard-Marchant, P., Sheppard, K., Reddy, T., Weckesser, W., Abbasi, H., Gohlke, C., Oliphant, T.E., 2020. Array programming with NumPy. Nature 585 (7825), 357–362.

Hill, A., Zhu, D., Wang, Y., 1995. The effect of wormholing on the fluid-loss coefficient in acid fracturing. SPE Prod. Facil. 10 (04), 257–264.

Hinde, A.L., 2004. Prinsas – a Windows-based computer program for the processing and interpretation of small-angle scattering data tailored to the analysis of sedimentary rocks. J. Appl. Crystallogr. 37 (6), 1020–1024.

Hoefner, M.L., Fogler, H.S., 1988. Pore evolution and channel formation during flow and reaction in porous media. AIChE J. 34, 45–54.

Izgec, O., Zhu, D., Hill, A.D., 2010. Numerical and experimental investigation of acid wormholing during acidization of vuggy carbonate rocks. J. Pet. Sci. Eng. 74 (1–2), 51–66.

Ji, Y., Radlinski, A.P., Blach, T., de Campo, L., Vu, P., Roshan, H., Regenauer-Lieb, K., 2022. How to avoid multiple scattering in strongly scattering SANS and USANS samples. Fuel 325, 124957.

Katz, A., Thompson, A., 1985. Fractal sandstone pores: implications for conductivity and pore formation. Phys. Rev. Lett. 54 (12), 1325.

Kelemen, P., Whitehead, J., Aharonov, E., Jordahl, K., 1995. Experiments on flow focusing in soluble porous media, with applications to melt extraction from the mantle. J. Geophys. Res. 100, 475–496.

Koeshidayatullah, A., Corlett, H., Hollis, C., 2021. An overview of structurally-controlled dolostone-limestone transitions in the stratigraphic record. Earth Sci. Rev. 220, 103751.

Ladd, A.J., Szymczak, P., 2021. Reactive flows in porous media: Challenges in theoretical and numerical methods. Annu. Rev. Chem. Biomol. Eng. 12, 543–571.

Li, W., Einstein, H.H., Germaine, J.T., 2019. An experimental study of matrix dissolution and wormhole formation using gypsum core flood tests: 1. Permeability evolution and wormhole geometry analysis. J. Geophys. Res. Solid Earth 124 (11), 11055–11073.

Lindner, P., Schweins, R., 2010. The D11 small-angle scattering instrument: a new benchmark for SANS. Neutron News 21 (2), 15–18.

Lipar, M., Szymczak, P., White, S.Q., Webb, J.A., 2021. Solution pipes and focused vertical water flow: Geomorphology and modelling. Earth Sci. Rev. 218, 103635.

Luquot, L., Gouze, P., 2009. Experimental determination of porosity and permeability changes induced by injection of CO_2 into carbonate rocks. Chem. Geol. 265 (1–2), 148–159.

McDuff, D.R., Shuchart, C.E., Jackson, S.K., Postl, D., Brown, J.S., 2010. Understanding wormholes in carbonates: Unprecedented experimental scale and 3-D visualization. J. Petrol. Technol. 62, 78–81.

Menke, H., Reynolds, C., Andrew, M., Nunes, J.P., Bijeljic, B., Blunt, M., 2018. 4D multi-scale imaging of reactive flow in carbonates: Assessing the impact of heterogeneity on dissolution regimes using streamlines at multiple length scales. Chem. Geol. 481, 27–37.

Merino, E., Banerjee, A., 2008. Terra rossa genesis, implications for karst, and eolian dust: A geodynamic thread. J. Geol. 116, 62–75.

Molins, S., Soulaine, C., Prasianakis, N.I., Abbasi, A., Poncet, P., Ladd, A.J., Vitalii Starchenko, S.R., Trebotich, D., Tchelepi, H.A., Steefel, C.I., 2020. Simulation of mineral dissolution at the pore scale with evolving solid-fluid interfaces: Review of approaches and benchmark problem set. Comput. Geosci. 25, 1285–1318.

Molins, S., Trebotich, D., Steefel, C.I., Shen, C., 2012. An investigation of the effect of pore scale flow on average geochemical reaction rates using direct numerical simulation. Water Resour. Res. 48, W03527.

Muljadi, B.P., Bijeljic, B., Blunt, M.J., Colbourne, A., Sederman, A.J., Mantle, M.D., Gladden, L.F., 2018. Modelling and upscaling of transport in carbonates during dissolution: Validation and calibration with NMR experiments. J. Contam. Hydrol. 212, 85–95.

Noiriel, C., Seigneur, N., Le Guern, P., Lagneau, V., 2021. Geometry and mineral heterogeneity controls on precipitation in fractures: An X-ray micro-tomography and reactive transport modeling study. Adv. Water Resour. 152, 103916.

Oliveira, R., Bijeljic, B., Blunt, M.J., Colbourne, A., Sederman, A.J., Mantle, M.D., Gladden, L.F., 2021. A continuous time random walk method to predict dissolution in porous media based on validation of experimental NMR data. Adv. Water Res. 149, 103847.

Ott, H., Oedai, S., 2015. Wormhole formation and compact dissolution in single-and two-phase CO_2-brine injections. Geophys. Res. Lett. 42, 2270–2276.

Petrus, K., Szymczak, P., 2016. Influence of layering on the formation and growth of solution pipes. Front. Phys. 3, 92.

Radlinski, A.P., 2006. Small-angle neutron scattering and the microstructure of rocks. Rev. Mineral. Geochem. 63 (1), 363–397.

Radlinski, A.P., Boreham, C., Lindner, P., Randl, O., Wignall, G., Hinde, A., Hope, J., 2000. Small angle neutron scattering signature of oil generation in artificially and naturally matured hydrocarbon source rocks. Org. Geochem. 31 (1), 1–14.

Radlinski, A.P., Ioannidis, M., Hinde, A., Hainbuchner, M., Baron, M., Rauch, H., Kline, S., 2004a. Angstrom-to-millimeter characterization of sedimentary rock microstructure. J. Colloid Interface Sci. 274 (2), 607–612.

Radlinski, A.P., Mastalerz, M., Hinde, A., Hainbuchner, M., Rauch, H., Baron, M., Lin, J., Fan, L., Thiyagarajan, P., 2004b. Application of SAXS and SANS in evaluation of porosity, pore size distribution and surface area of coal. Int. J. Coal Geol. 59 (3–4), 245–271.

Rowan, G., 1959. Theory of acid treatment of limestone formations. J. Inst. Pet. 45 (431), 321.

Sander, R., 2015. Compilation of Henry's law constants (version 4.0) for water as solvent. Atmos. Chem. Phys. 15 (8), 4399–4981.

Selvadurai, A., Couture, C.-B., Rezaei Niya, S., 2017. Permeability of wormholes created by CO_2-acidized water flow through stressed carbonate rocks. Phys. Fluids 29 (9), 096604.

Smith, M., Sholokhova, Y., Hao, Y., Carroll, S., 2013. CO_2-Induced dissolution of low permeability carbonates. Part I: Characterization and experiments. Adv. Water Res. 62, 370–387.

Snippe, J., Berg, S., Ganga, K., Brussee, N., Gdanski, R., 2020. Experimental and numerical investigation of wormholing during CO_2 storage and water alternating gas injection. Int. J. Greenh. Gas Control 94, 102901.

Soulaine, C., Roman, S., Kovscek, A., Tchelepi, H.A., 2017. Mineral dissolution and wormholing from a pore-scale perspective. J. Fluid Mech. 827, 457–483.

Spiegelman, M., Kelemen, P., Aharonov, E., 2001. Causes and consequences of flow organization during melt transport: the reaction infiltration instability in compactable media. J. Geophys. Res. 106, 2061–2077.

Steefel, C.I., Molins, S., Trebotich, D., 2013. Pore scale processes associated with subsurface CO_2 injection and sequestration. Rev. Mineral. Geochem. 77 (1), 259–303.

Studencki, W., 1988. Facies and sedimentary environment of the Pinczow limestones (middle miocene; holy cross mountains, central Poland). Facies 18 (1), 1–25.

Szymczak, P., Ladd, A.J.C., 2009. Wormhole formation in dissolving fractures. J. Geophys. Res. 114, B06203.

Szymczak, P., Ladd, A.J.C., 2014. Reactive infiltration instabilities in rocks. Part 2. Dissolution of a porous matrix. J. Fluid Mech. 738, 591–630.

Tengattini, A., Lenoir, N., Andò, E., Giroud, B., Atkins, D., Beaucour, J., Viggiani, G., 2020. Next-Grenoble, the neutron and X-ray tomograph in Grenoble. Nucl. Instrum. Methods. Phys. Res. A 968, 163939.

Upadhyay, V.K., Szymczak, P., Ladd, A.J.C., 2015. Initial conditions or emergence: What determines dissolution patterns in rough fractures? J. Geophys. Res.: Solid Earth 120 (9), 6102–6121.

Van der Walt, S., Schönberger, J.L., Nunez-Iglesias, J., Boulogne, F., Warner, J.D., Yager, N., Gouillart, E., Yu, T., 2014. Scikit-image: image processing in python. PeerJ 2, e453.

Virtanen, P., Gommers, R., Oliphant, T., Haberland, M., Reddy, T., Cournapeau, D., Burovski, E., Peterson, P., Weckesser, W., Bright, J., 2020. Scipy 1.0: fundamental algorithms for scientific computing in Python. Nat. Methods 17 (3), 261–272.

Yang, X., Scheibe, T.D., Richmond, M.C., Perkins, W.A., Vogt, S.J., Codd, S.L., Seymour, J.D., McKinley, M.I., 2013. Direct numerical simulation of pore-scale flow in a bead pack: Comparison with magnetic resonance imaging observations. Adv. Water Res. 54, 228–241.